Colliding Pulse Mode Locking and Nonequilibrium Carrier Dynamics within Vertical External-Cavity Surface-Emitting Lasers

S.A. McLaren[1,2,*] I. Kilen,[3] and J.V. Moloney[2,4]

[1]*Lawrence Livermore National Laboratory, 7000 East Ave., Livermore, California 94550, USA*

[2]*Arizona Center for Mathematical Sciences, University of Arizona, 1630 East University Boulevard, Tucson, Arizona 85721-0094, USA*

[3]*Norwegian Defence Research Establishment (FFI), Kjeller, Norway*

[4]*James C. Wyant College of Optical Sciences, University of Arizona, 1630 East University Boulevard, Tucson, Arizona 85721, USA*

The complex nonlinear dynamics of colliding counterpropagating ultrashort laser pulses circulating in a vertical external-cavity surface-emitting ring laser cavity are captured by a first-principles quantum-mechanical microscopic model coupled to an intracavity beam propagator. Our numerical simulations establish that overall mode locking stability is sensitive to relative phases and delays of the pulses impinging on the semiconductor saturable absorber mirror. Delay offsets of the counterpropagating pulses lead to asymmetric carrier recovery and instability, often leading in turn to single unidirectional circulating pulses. Although computationally challenging, we also include transverse effects and show that the influence of interference patterns from spatial gratings written by the counterpropagating pulses is significant in stabilizing the modelocked pulses.

I. INTRODUCTION

Colliding pulse mode locking (CPM) has been studied extensively as a means of producing ultrafast pulses since its initial application to dye lasers [1]. The modern vertical external-cavity surface-emitting laser (VECSEL), sometimes referred to as a semiconductor disc laser, provides a research test bed for CPM [2,3]. These lasers, described by Kuznetsov *et al.* in 1997 [4], are a modern source for compact high-brightness, high-beam-quality, single-mode continuous-wave and ultrafast laser pulses. Due to advanced bandgap engineering technologies, VECSELs can operate across much of the electromagnetic spectrum [5,6]. Particular applications include supercontinuum generation [7], sodium guide star generation [8], ultrafast laser ablation [9], and single- and dual-frequency comb generation [10]. For a more thorough review of VECSEL technologies and applications see Keller *et al.* [11,12], Rahimi-Iman [13], or Guina [14].

The shortest uncompressed pules from a VECSEL to date were obtained using a colliding pulse ring cavity setup [15]. These setups utilize a surface-emitting multiple quantum well (MQW) based semiconductor gain chip, ubiquitous in VECSEL operation, a semiconductor saturable absorber mirror (SESAM), and an output coupler

(OC) [16]. These components are arranged to form a ring, shown schematically in Fig. 1. The angles and arm lengths are shown symmetrically, though an actual cavity can tune these parameters dependent on desired cavity lengths, lab space, and the inclusion of additional optical elements.

VECSEL ring cavities are more complicated than passively modelocked V-cavities. The more complicated geometry allows a single pass over the gain chip per round trip, as opposed to the double pass in a V-cavity. This minimizes the largest source of dispersion in the cavity. Additionally, the bidirectional cavities naturally stabilize to have counterpropagating pulses which collide on the SESAM, minimizing the amount of pulse energy required to bleach the SESAM. Because of this, the absorption can be more readily bleached at lower energy fluences, minimizing the degradation of the SESAM chip, typically caused by two-photon absorption [17,18]. The physics involved in mode locking in such ring cavities is nontrivial, involving a dynamical competition between ultrafast nonequilibrium carrier kinetic hole burning and filling, resulting nonlinear gain and loss, spatial gratings written by counterpropagating pulses impinging on the SESAM, and external cavity geometry influences. The interplay of all these intrinsic and cavity-based mechanisms has never been studied at this microscopic level. In particular, the influence of higher-order spatial gratings directly relevant
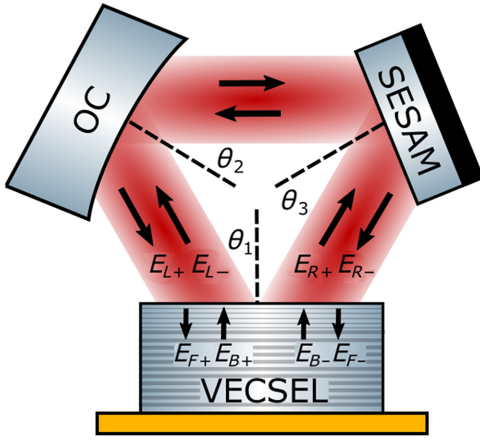
---

*smclaren@math.arizona.edu

FIG. 1. Generic ring cavity setup with output coupler (OC), SESAM, and VECSEL gain chip, shown symmetrically. Four copropagating fields are present within non-normal incidence–exhibiting components.

in CPM VECSELs [19] on stabilizing pulses has not been demonstrated in such setups. In this article, we utilize a first-principles quantum-mechanical coupled VECSEL model to highlight the rich and varied physics underlying CPM. We highlight broad ring cavity behaviors that drive these remarkably powerful, and robustly stable, cavities. These results should inform both future experimental ring cavity setups and numerical studies utilizing simpler models.

There are many rate- or quasiequilibrium-based numerical laser models employed to study such laser geometries, dating back to the Haus master equations [20]. Tools used range from simple gain saturation models [21], via delay differential equation models which phenomenologically model individual components within the laser cavity [22–24], to more complicated models that incorporate direct material responses and coherent effects [25,26]. These are often used to predict and guide experimental design but have also been used analytically to demonstrate macroscopic gain dynamics, including pulse clustering [27]. These approaches have been important in both elucidating global behavior and allowing the rapid development of VECSEL technologies and capabilities. The primary drawback is the need for extensive experimentally driven parameterization, such as saturation fluences and Fermi-Dirac quasiequilibrium carrier distributions. Including a spectral response in macroscopic models adds an additional complexity in the form of either restrictive assumptions or experimentally derived gain filters and dispersion functions [28]. The consequence is the loss of robustness, parameter availability, and predictive capability as experiment-specific parameters need to be recalculated whenever the experimental setup is changed. Thus, in tandem with simpler macroscopic models, it is useful to have a higher-fidelity model

both to inform updates of the macroscopic quantities and to investigate more fundamental physical behaviors such as destabilization, pulse molecule formation, and complex inhomogeneous spectral broadening and shifting. A microscopic- based approach, although more computationally challenging, provides a direct predictive picture that utilizes rigorous physics capturing the precise details of the semiconductor gain and absorbing structure. From these simulations, dispersion, gain, and saturation can easily be computed for use in broader low-fidelity model sweeps [29]. For example, ultrafast carrier-carrier scattering processes impose a boundary between a pulse experiencing a low effective gain (femtosecond pulses), when scattering is too slow to refill a burned kinetic hole, and enhanced effective gain for longer duration pulses (picosecond) where excess carriers can refill the hole and enhance the stimulated generation of additional photons. Here we present such a first- principles microscopic model in tandem with light propagation macroscopic models to develop fundamental theories and intuition as a means to inform simpler models, alongside future experimental setups.

II. MODEL

The transverse Maxwell semiconductor Bloch equations (TMSBE) model couples together a pseudospectral beam propagation method (BPM) and a transfer matrix method to a first- principles quantum-mechanical description of the semiconductor quantum wells. The one-dimensional model has been used extensively to design gain chips and further understanding of the fundamental physics [30,31]. The transverse model expands on this and has been used to study transverse field instabilities as well as mode locking behaviors in V-cavity VECSELs [32,33]. This article utilizes this model to characterize the driving physics and demonstrate optimization criteria for CPM operation within ring cavity VECSELs. Mode locking is captured from spontaneous emission by discretizing the various material layers and air regions and iterating the propagation and nonlinear interactions in a split-step manner.

The pseudospectral BPM allows the propagation of the field within the various components of the model as shown in the following equation:

$$E(\mathbf{r}, z) = FFT^{-1}\left(e^{F(k_x, z)} \cdot E(\mathbf{r}, 0)\right). \quad (1)$$

The particular propagator used, $F(\mathbf{k}, z)$, is derived as a Fourier transform of Green's function for the scalar wave equation,

$$F(\mathbf{k}, z) = iz\left(\sqrt{k_0^2 - \mathbf{k}^2} - k_0\right), \quad (2)$$

for a central and distributed wavenumbers k_0, k, respectively. Boundary conditions for Maxwell's equations lead to a normal incidence transfer matrix that relates the incoming and outgoing electric fields based on Fresnel reflection and transmission coefficients [34]. Each material layer within the model is treated as homogeneous and isotropic, numerically instantiated from the OC, through the various materials and layers of the setup in a linear fashion, with periodic boundary conditions used at the final OC interaction so that the field recirculates. The OC is modeled as a 1% loss in intensity at each encounter. Material layers are labeled in increasing order. For the interface between layers j and $j + 1$ with forward (backward) moving fields expressed by $+(-)$ respectively and frequency-independent refractive indices n_j and n_{j+1}, the electric field transfer matrix becomes

$$(n_j + n_{j+1}) \begin{bmatrix} E_{j+1}^+ \\ E_j^- \end{bmatrix} = \begin{bmatrix} 2n_j & n_{j+1} - n_j \\ n_j - n_{j+1} & 2n_{j+1} \end{bmatrix} \begin{bmatrix} E_j^+ \\ E_{j+1}^- \end{bmatrix} - \mu_0 c_0 \frac{\partial}{\partial t} P(z, t) \quad (3)$$

for the vacuum permeability, μ_0. The macroscopic polarization density, $P(z, t)$, is only nonzero when the field crosses over a quantum well [35]. This is generalized in the non-normal incidence case to accommodate oblique transmission and reflection as well as incoming and outgoing fields along distinct paths [33]. The non-normal incidence is captured using a hybrid approach, the field is propagated to the average distance of the tilted plane, and then the appropriate additional path length is added as a delay along the transverse dimension. The astigmatism induced by the non-normal incidence, as well as the transversally dependent diffraction, are neglected as they have minimal influence on the particular setups studied. A boundary guard is used to minimize backreflection from any outgoing fields.

Within rate-based models, the macroscopic polarization density is frequently adiabatically eliminated, and expressed in terms of the electric field. In the TMSBE, it is numerically integrated from the microscopic polarization densities, obtained by numerically coupling the semiconductor Bloch equations (SBE). The general two-parabolic-band SBE are

$$\frac{\partial}{\partial t} p_k = -i\omega_k p_k - i\Omega_k(n_k^e + n_k^h - 1) + \frac{\partial}{\partial t} p_k|_{\text{scatt}},$$

$$\frac{\partial}{\partial t} n_k^{e(h)} = i\left[\Omega_k p_k^* - \Omega_k^* p_k\right] + \frac{\partial}{\partial t} n_k^{e(h)}|_{\text{scatt}}, \quad (4)$$

where the generalized single particle energies, $\hbar\omega_k$, and Rabi frequencies, Ω_k, are defined as

$$\hbar\omega_k = \frac{\hbar^2 k^2}{2m_r} - \sum_{q \neq k} V_{|k-q|}(n_k^e + n_k^h),$$

$$\Omega_k = \frac{1}{\hbar}\left(d_{\text{cv}}\mathcal{E}(t) + \sum_{q \neq k} V_{|k-q|}p_q\right). \quad (5)$$

Here, m_r is the reduced mass of the electron hole pair, V is the screened Coulomb potential, and d_{cv} is the dipole transition matrix element for the transition between conduction and valence bands. Within the classical optical Bloch equations, which describe a two-level oscillator excited by an incident field, the single particle energy characterizes the natural frequency of the driven system, whereas the Rabi frequency describes the oscillations driven by the incident field. The SBE generalize these concepts through the Coulomb potential, coupling together the oscillators associated with any transition from one band to the next. Although a continuum in reality, these transitions are discretized to 100 points for these results.

Note the population inversion, $n_k^e + n_k^h - 1$. This quantity most readily indicates the growth of cavity pulses through the burning of *kinetic holes* about particular momentum states [35] and has a direct relation to the macroscopic population inversion. When the population inversion is positive (negative) the system will exhibit gain (absorption) for that particular state. However, the system as a whole may still exhibit a net energy loss. As the carriers are fully depleted in a certain kinetic region, population inversion *bleaching* occurs. The region no longer exhibits gain (absorption) until the carriers recover. Capturing the full particle scattering is not possible. A common and successful approximation of the full scattering for this system is done at the second Born level which goes beyond Hartree-Fock and captures carrier-carrier scattering (electron-electron, hole-hole, phonon) [29]. Inclusion of this scattering is extremely computationally demanding, requiring multidimensional matrix sums at each step. An earlier study including second Born scattering shows that the scattering rates are strongly nonuniform in carrier momentum. However, it has been verified that replacement of this scattering time by an average (constant value of 100 fs) can capture the qualitative evolving dynamical structure of the pulse as it builds up from noise or a seed to a stable (unstable) modelocked state. So in this paper we will approximate this scattering using multiple effective recovery rates,

$$\frac{\partial}{\partial t} p_k = -i\omega_k p_k - i\Omega_k(n_k^e + n_k^h - 1) + \Gamma_{\text{deph}} + \Lambda_{\text{spont}}^p,$$

$$\frac{\partial}{\partial t} n_k^{e(h)} = i\left[\Omega_k p_k^* - \Omega_k^* p_k\right] + \Gamma_{\text{scatt}} + \Lambda_{\text{spont}}^n + \Gamma_{\text{fill}}. \quad (6)$$

The polarization dephasing is modeled using a single phe-nomenological decay rate derived from simulations using scattering approximations on the second Borne-Markov level [29],

$$\Gamma_{\text{deph}} = -\frac{1}{\tau_{\text{deph}}} p_k, \tag{7}$$

where $\tau_{\text{deph}} = 47$ fs is the characteristic material polarization dephasing time. Within the charge carrier equations, the scattering terms are approximated using dual recovery rates: a slow recovery to a background distribution,

$$\Gamma_{\text{scatt}} = -\frac{1}{\tau_{\text{scatt}}} \left(n_k^{e(h)} - f_k^{e(h)} \right), \tag{8}$$

and a rapid recovery to an instantaneous computed distribution,

$$\Gamma_{\text{fill}} = -\frac{1}{\tau_{\text{fill}}} \left(n_k^{e(h)} - F_k^{e(h)} \right). \tag{9}$$

Here, $f_k^{e(h)}$ is a background Fermi distribution and $F_k^{e(h)}$ are dynamically computed based on the current total density and temperature of the system [29]. The slow scattering times are taken as $\tau_{\text{scatt}} = 20$ ps, 1 ps for gain chip and SESAM quantum wells (QWs), respectively. The scattering times here are scaled down for smaller cavities used herein to mimic recovery effects within larger cavities. The slow timescale can readily be modeled using quasiequilibrium macroscopic rate approaches where individual gain exponentially recovers. However, the rapid recovery, set to $\tau_{\text{fill}} = 100$ fs, is not captured in these models. By allowing carriers to be driven far from Fermi distributions, dynamically evolving inhomogeneous gain is accurately captured along the duration of the pulse. Thus the generation of temporal and transverse substructures and instabilities can be accurately modeled with high fidelity. Previous work has shown how this model can be used to generate spectrally broad and inhomogeneous gain profiles for use in simpler models [36].

These three components, intramaterial propagation, material boundary transfer matrices, and highly localized nonlinear gain/absorption, are iteratively coupled together to form the TMSBE and capture the transient and asymptotic nonequilibrium carrier and pulse dynamics within modelocked VECSELs [32]. Previous work has introduced the capability of modeling non-normal incidence structures through an appropriate reference frame transform [33]. Part of this transform includes expanding the SBE into Fourier modes to capture appropriately directed stimulated emission as well as to properly exclude light walkoff which results from interacting pulses and four-wave mixing. The field, microscopic polarizations, and occupation numbers are expanded as

$$E_{\text{QW}} = \sum_{j=1}^{4} E_j e^{i\mathbf{Q_j} \cdot \mathbf{r}}, \tag{10}$$

$$n_k^{e(h)} = \sum_{m=-\infty}^{\infty} n_{k,m} e^{im\mathbf{q} \cdot \mathbf{r}}, \tag{11}$$

$$p_k = \sum_{m=-\infty}^{\infty} p_{k,+,m} e^{i\mathbf{Q} \cdot \mathbf{r} + im\mathbf{q} \cdot \mathbf{r}} \tag{12}$$

$$+ \sum_{m=-\infty}^{\infty} p_{k,-,m} e^{-i\mathbf{Q} \cdot \mathbf{r} + im\mathbf{q} \cdot \mathbf{r}}, \tag{13}$$

$$\mathbf{Q}_{1(2)} = \mathbf{Q} \mp \mathbf{q}, \quad \mathbf{Q}_{3(4)} = -\mathbf{Q} \mp \mathbf{q}, \tag{14}$$

where, $\mathbf{Q}$ is normal to the semiconductor interface and $\mathbf{q}$ captures the angle of incidence relative to this normal. The four fields correspond to the incoming and outgoing field along the left and right arms of a non-normal incidence interface. These are numerically tracked throughout any structure that has non-normally incident fields. The forward and backward field- induced material polarization waves are labeled as $+$ and $-$, respectively.

From here, we introduce these expansions into the SBE. Collecting only terms which contribute to the particular directions leads to the expanded SBE. The general forms of the polarization equations are symmetric in the forward and backward directions. For the forward equation,

$$\frac{\partial}{\partial t} p_{k,+,m} = \Lambda_{\text{spont}}^p - \frac{1}{\tau_{\text{deph}}} p_{k,+,m}$$

$$- i \left[\frac{\epsilon_r}{\hbar} p_{k,+,m} - \frac{1}{\hbar} \sum_{q,j} V_{|k-q|} (n_{q,j}^e + n_{q,j}^h) p_{k,+,m-j} \right]$$

$$- i \left[\frac{d_{\text{cv}}}{\hbar} \left[E_1(t) (n_{k,m-1}^e + n_{k,m-1}^h - \delta_{m,1}) \right. \right.$$

$$+ E_2(t) (n_{k,m+1}^e + n_{k,m+1}^h - \delta_{m,-1}) \right]$$

$$+ \frac{1}{\hbar} \sum_{q,j} V_{|k-q|} p_{q,+,j} \left(n_{k,m-j}^e + n_{k,m-j}^h - \delta_{j,m} \right) \right]. \tag{15}$$

Note that although all terms are coupled through the renormalizations and higher-order occupation numbers, the forward equations only explicitly contain the two forward-moving fields, $E_{1,2}(t)$. This holds likewise for the backward polarizations. The general form for the expanded

electron (hole) occupation numbers is

$$
\begin{aligned}
\frac{\partial}{\partial t} n_{k,m}^{e(h)} = {}& \Lambda_{\mathrm{spont}}^{n} \\
& - \frac{1}{\tau_{\mathrm{scatt}}} \left(n_{k,m}^{e(h)} - F_{k,m}^{e(h)} \right) - \frac{1}{\tau_{\mathrm{fill}}} \left(n_{k,m}^{e(h)} - f_{k,m}^{\,e(h)} \right) \\
& + i \Bigg[\frac{d_{\mathrm{cv}}}{\hbar} \left(E_1(t) p_{k,+,-m+1}^{*} + E_2(t) p_{k,+,-m-1}^{*} \right. \\
& \quad + E_3(t) p_{k,-,-m-1}^{*} + E_4(t) p_{k,-,-m+1}^{*} \Big) \\
& \quad + \frac{1}{\hbar} \sum_{q,j} V_{|k-q|} \left(p_{q,+,j} p_{q,+,-m+j}^{*} + p_{q,-,j} p_{q,-,-m+j}^{*} \right) \Bigg] \\
& - i \Bigg[\left(\frac{d_{\mathrm{cv}}}{\hbar} E_1(t)^{*} p_{k,+,m+1} + E_2(t)^{*} p_{k,+,m-1} \right. \\
& \quad + E_3(t)^{*} p_{k,-,m-1} + E_4(t)^{*} p_{k,-,m+1} \Big) \\
& \quad + \frac{1}{\hbar} \sum_{q,j} V_{|k-q|} \left(p_{q,+,j}^{*} p_{q,+,m+j} + p_{q,-,j}^{*} p_{q,-,m+j} \right) \Bigg].
\end{aligned}
\tag{16}
$$

To ensure that the expanded occupation numbers are real, the condition $n_{k,m}^{e(h)} = \left(n_{k,-m}^{e(h)} \right)^{*}$ is enforced. These terms couple in alternating parity such that only even occupation number modes and odd polarization modes are significant.

The directed macroscopic polarization densities are found using the appropriate density of states to integrate

$$
P_{+(-),m}(\mathbf{r}, t) = \sum_{k} d_{\mathrm{cv}} p_{k,+(-),m}.
\tag{17}
$$

III. SINGLE-PASS RESULTS

Simulations of mode locking typically involve tens of thousands of passes within the cavity before the pulse reaches a dynamical asymptotic state. To hasten simulation convergence, we can introduce a weak seed pulse to initiate the simulation. It is helpful therefore to get a picture of how significant macroscopic effects such as relative phase or delay of the pulses colliding on the SESAM can influence the final state of the system in full simulations. If a single pulse were to strike the SESAM it would be sufficient to consider just the lowest (zero) order spatial grating terms, $n_{k,0}^{e(h)}, p_{k,\pm,\pm1}$. However, for colliding counterpropagating pulse operation, the fields mix and the higher-order spatial grating terms become relevant. Fortunately, it is sufficient to include just the next-order contributions to the populations and polarizations as their relative strength drops off rapidly with increasing order. To demonstrate this, we consider two 100 fs pulses with amplitudes of 5×10^6 V/m, colliding at non-normal incidence, $\theta = 2°$, on a single unpumped QW, $n_0 = 5.0 \times 10^{14}$ m^{-2}, shown in Fig. 2. This carrier density (or equivalently, in this case

pulse intensity) is just at the level needed to reach inversion in the SESAM QW under continuous wave excitation. Therein, the columns from left to right are the population inversion, zeroth-order electron occupation number and second-order (grating) electron occupation number, respectively. The population inversions are shown in units of inverse lattice constants, a_0. The relative phases of the incident pulses are such that the first row depicts results for which incident colliding pulses are in phase, while the second row depicts results when the two colliding pulses are 180° out of phase. Figures 2(a) and 2(d) show the population inversion for these simulations. As the pulses are incident on the QW, they excite carriers through the absorption of photons. This creates peaks in the population inversions and drives the carriers far from Fermi distributions. As the pulses leave, the carriers rapidly recover toward instantaneous hot Fermi distributions and slowly recover toward background Fermi distributions at the lattice temperature. Notice that the peak in Fig. 2(a) for in-phase colliding pulses drives the momentum resolved inversion closer to the transparency point whereas the out-of-phase case in Fig. 2(d) results in significantly less bleaching. Interestingly, the zeroth-order electron occupation numbers, shown for the left-arm forward direction, for the two cases, Figs. 2(b) and 2(e), are nearly identical. Thus, the stimulated emission along the primary directions is independent of the relative phases of the incident colliding pulses. However, the total carrier population is highly sensitive to this phase. The second-order grating electron occupation numbers, again shown for the left-arm forward direction, are shown in Figs. 2(c) and 2(f). Note that they are near perfect reflections about the horizontal momentum axis. These are not physical quantities in themselves but do have physical implications, with the in-phase contribution adding to the inversion while the out-of-phase term further decreases the dynamic inversion. This simple single-pass colliding pulse example demonstrates that the relative phase of colliding pulses has a dramatic influence on the total carrier depletion, or growth.

It is clear that the relative phases of the pulses have a dramatic influence on carrier dynamics, but less clear what relative phase is likely to be observed during a mode locking experiment. Figure 3 shows a similar study using the transverse model. Two 100 fs pulses with amplitudes of 1×10^7 V/m are propagated into a SESAM at a $\theta = 1°$ angle. These pulses were either initialized with an equal phase or 180° out of phase. The resulting intensity profiles for the in-phase and out-of-phase pulses within the QW are shown in Figs. 3(a) and 3(b), respectively. Both the interference pattern and phase relationship are clearly evidenced by the oscillating peaks. Note that the strength of the peaks is not affected by the phase relationship. The phase merely results in a translation of the peaks. Figures 3(c) and 3(d) show the resulting integrated electron density within the SESAM QW near the pulse peaks at
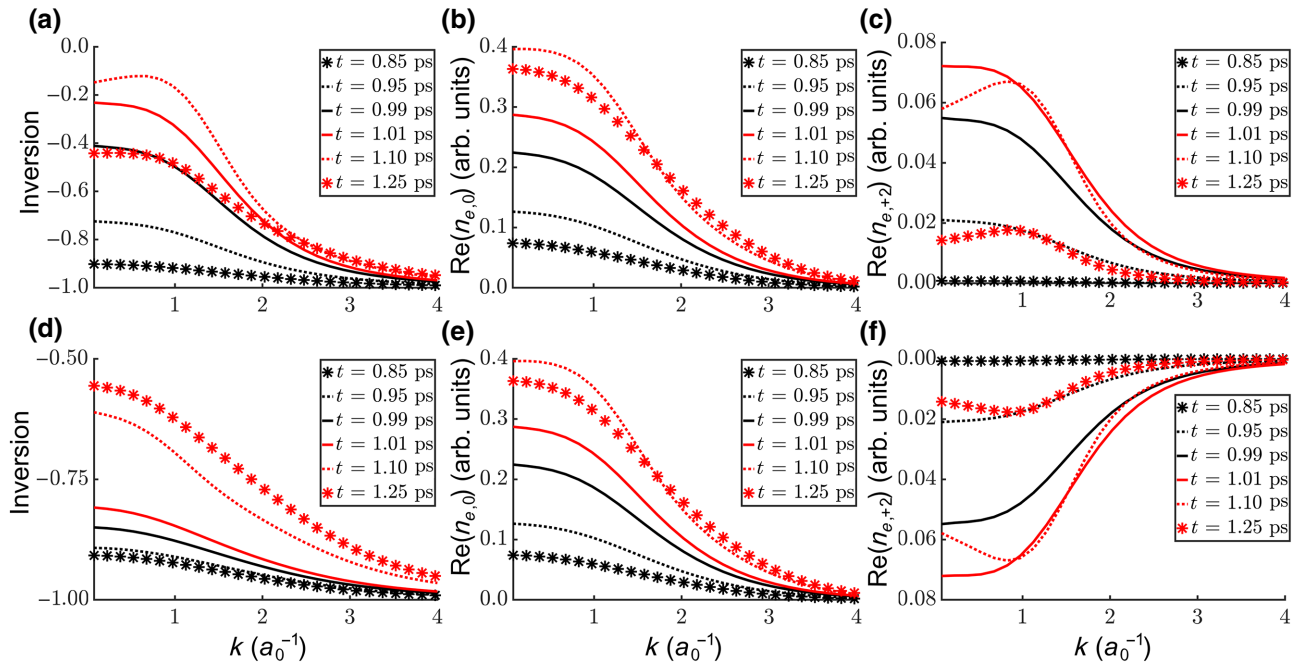
FIG. 2.   Low-density, 5.0×10^{14} m^{-2}, carrier population dynamics for in-phase (a)–(c) and out-of-phase (d)–(f) simulations with two incident 100 fs, 5.0×10^6 V/m colliding pulses, with peaks at 1 ps. The total population inversions (a),(d) highlighting the significant difference in inversion that results from in-phase versus out-of-phase pulses, respectively. The lowest-order electron occupation number which directly contributes to the fields (b),(e) and real component of the second-order electron occupation number (c),(f) and shows that this difference comes almost entirely from the higher-order grating terms.

t_0 for the in-phase and out-of-phase simulations, respectively. The pulses enter the QW and begin exciting carriers, with peak carrier densities 10 fs after the peak of the colliding pulses. The generation of excited carriers along the transverse axis directly corresponds with the total incident field intensity, with clearly evidenced interference fringes along with additional side bands. Five hundred femtoseconds after the pulse peak, the interference fringes have almost entirely disappeared from the carrier density, which then slowly recovers back to its background value. From this we see that the higher-order interference fringes dissipate rapidly relative to the lowest-order terms. Note that both the magnitude of the density peaks and the resulting recovered carrier density at $t_0 + 500$ fs are relatively independent of the phase relationship. Figures 3(c) and 3(d) both support a lower required saturation fluence during CPM relative to single-pulse mode locking. Integrated quantities like these can be used to compare peak and residual carrier densities and for generating gain profiles within simpler models [22,23]. In addition, they demonstrate that the transverse location of peak absorption is highly dependent on the phase relationship between the pulses. Because the cavity geometry strongly dictates the transverse width of the pulse, out-of-phase pulses, where the pulses experience weak absorption at their peaks, first saturate the SESAM at much higher fluences than do in-phase pulses. For strong pumping conditions this would be a much less

stable setup, whereas for weak pumping conditions this would be more stable. Thus, the phase relationship is not necessarily static and is related to strength of the pumping with decreased correlation for higher angles, and lower foci on the SESAM. This implies increased pulse stability at lower angles and tighter foci as the phase relationship is less susceptible to perturbations.
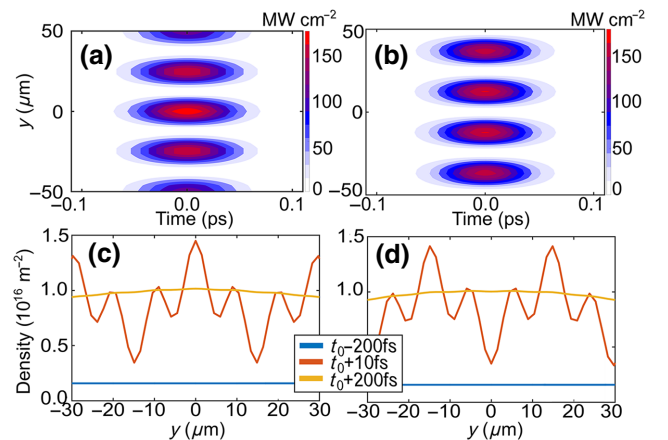

FIG. 3.   In-phase (left column) and out-of-phase (right column) colliding pulse operation. Pulse intensities at the SESAM QW (a),(b) and resulting electron densities within the QW taken before, during, and after the incident pulse (c),(d).
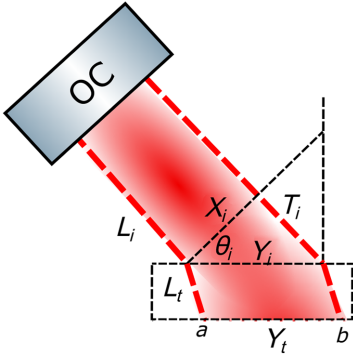
FIG. 4. Non-normal incidence induced transverse optical path length delay.

FIG. 5. First (a) and third (b) spatial order macroscopic polarizations for variable delays for colliding 100 fs, 2.0×10^5 V/m pulses indicating no saturation and Gaussian shape of grating terms that grows with increasing overlap. First (c) and third (d) spatial order macroscopic polarizations for variable delays for colliding 100 fs, 1×10^7 V/m pulses indicating strong saturation with increasing overlap accompanied by multipeaked grating terms.

Another important consideration within CPM setups is the temporal delay between counterpropagating pulses. Colliding pulse mode locking relies on the minimization of absorption induced when the pulses are coincident on the SESAM. Understanding the dynamics for varying relative pulse delays is critical to understanding why pulses tend dynamically toward a maximum temporal overlap. Further, pulses with nonzero transverse widths which collide at an angle, as is the case in non-normal incidence CPM setups, will be temporally offset, due to varying optical path length across the beam as depicted in Fig. 4 [33]. The length T_i is determined by the following geometric relationship:

$$T_i = X_i \tan(\theta_i). \tag{18}$$

Note that for small angles, this path length difference grows linearly across the transverse beam from center to wings and can lead to temporal delays that are much longer than the pulse length. Thus, Gaussian pulses colliding at an angle will see diminishing overlap extending outward along their transverse profiles. It is not clear a priori what effect this increasing delay might have on reshaping the transverse profile of the beam. Figure 5 shows the macroscopic polarization for colliding pulse setups when a delay is introduced between the pulses, within a one-dimensional single pass setup. Two 100 fs pulses, with peak amplitudes of either 2.0×10^5 V/m [Figs. 5(a) and 5(b)] or 1.0×10^7 V/m [Figs. 5(c) and 5(d)] were incident on an unpumped QW, $n_0 = 5.0 \times 10^{14}$ m^{-2}, one from each arm, with a variable delay between them. The first-order polarization for weak pulses [Fig. 5(a)] is unaffected by the delay between the pulses, whereas the third-order polarization [Fig. 5(b)] grows monotonically stronger as the delay decreases. However, the third-order polarization remains fundamentally Gaussian in form, indicating little to no saturation of the SESAM. Notice the three orders of magnitude difference in scale, indicating very little contribution from this term. Thus, the delay has only minimal effect as the pulses are building, and the setup is primarily linear until it begins to saturate. Under saturation conditions,
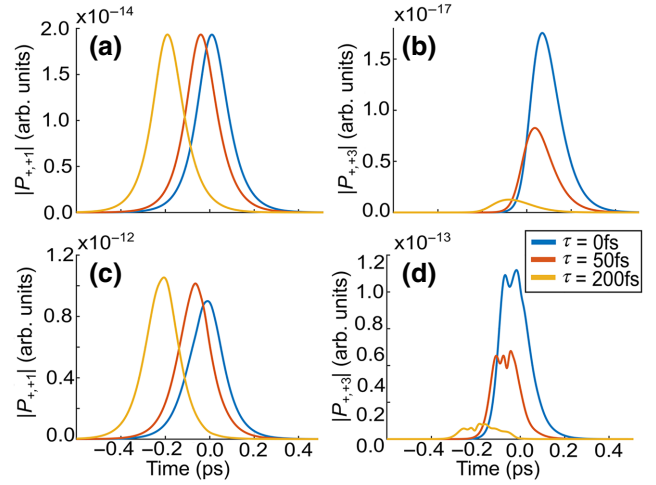
the first-order polarization [Fig. 5(c)] shows a noticeable monotonic decrease in amplitude with decreasing delay. The third-order polarization [Fig. 5(d)] again shows a monotonic growth with decreasing delay, but also exhibits a changing profile and variable number of peaks. The scales of Figs. 5(c) and 5(d) differ by only a single order of magnitude, indicating a much stronger nonlinear relationship, with significant absorber saturation. This saturation happens most quickly for pulses that collide perfectly, for example in a CPM setup at the center of the beam, driving ring cavities toward CPM. Additionally, the saturation occurs more slowly, moving outwards along the transverse dimension. Thus, operating with larger angles, and larger beam profiles, will naturally lead to higher variations in saturable absorption along the transverse dimension. Experimentally, this implies that the shortest, most uniform pulses are obtainable for near-normal angles of incidence with tight foci.

As demonstrated, the carrier dynamics with a SESAM under colliding pulse conditions are highly nonlinear and strongly depend on the relative phase and timing of the incident pulses. This is a strong justification for resolving the transverse nonequilibrium carrier dynamics within the system as the interference fringes contribute dramatically to the gain/loss in the system and are only present on the timescale of the pulse duration.

IV. MODE LOCKING RESULTS

In this section we present mode locking results in one- and two-dimensional studies which highlight the
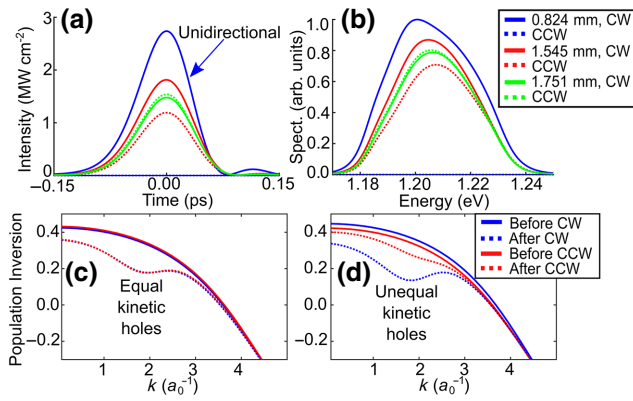
FIG. 6. Shifting output coupler to gain chip length simulations shown through (a) output pulse intensity, and (b)converged pulse spectra indicating a shifting of energy from equal-strength pulses to unidirectional operation accompanied by a broadening (narrowing) of the spectrum. Population inversions within the SESAM QW for the (c) 1.751 mm simulation, highlighting consistent kinetic hole burning and recovery in both directions, and for the (d) 1.545 mm simulation, demonstrating the converged effect of different recovery times.

complex pulse behaviors seen in CPM setups as they are driven by the underlying carrier dynamics in this nonlinear system. Due to the complex nature of these simulations, numerous one-dimensional studies are used to highlight broad behaviors and refine interesting studies for individual two-dimensional simulations. Utilizing one-dimensional studies, we justify the placement of the gain chip near a quarter round trip from the SESAM as this allows the symmetric recovery of carriers on successive pulse passes. We show the complex spectral and spatial behaviors found in semistable overpumped cavities which are shown to exhibit both distinct spectral peaks for the counterpropagating pulses and transient unidirectionality. Two-dimensional studies are used to highlight the strength of the carrier gratings, how they contribute to path length biases, and that CPM setups operate optimally with minimal angles of incidence on the SESAM.

A. One-dimensional mode locking studies

It was previously argued that the optimal location for the gain chip is a quarter round trip from the SESAM as this allows the most gain recovery per pulse pass [2,3]. In addition, it was argued that pulses have a natural tendency to balance each other through gain competition. The nonlinear role that chip position plays in the final modelocked pulses is shown. Although gain competition is strongly present, this does not naturally balance pulses in each direction. Consider a cavity with a constant total cavity length of 6.7 mm, where the gain chip is translated between the output coupler and the SESAM. Using a constant angle

of incidence, $\theta = 2°$, for both chips, and a background density of 2.5×10^{16} m^{-2}, Fig. 6 shows the converged output for simulations with variable output coupler to SESAM lengths. Note that at $L = 1.648$ mm, the gain chip is a quarter round trip from the SESAM, the proposed ideal distance. Figure 6(a) shows the converged output pulse intensities for these simulations, for both the clockwise (CW) and counterclockwise (CCW) output beams. When the gain chip is closest to the OC, 0.824 mm, there is only a single pulse within the converged simulation, propagating in the CW direction. As the chip is moved further toward the SESAM, the CCW pulse grows stronger until it surpasses the CW pulse. This trend demonstrates that gain competition does not readily balance the pulses. Rather, the relative intensities of the pulses are highly sensitive to the position of the gain chip within the cavity. The total output energy is much larger near the symmetry point in the cavity, confirming the ideal chip placement at approximately one fourth of a round trip from the SESAM. Figure 6(b) shows the converged pulse spectra, illustrating shifting spectral peaks with changing lengths. For the shortest length, the single CW spectral peak is dramatically broadened and severely shifted toward lower energies. As the chip is moved, the CW peak narrows and shifts to higher energies, and the CCW peak grows and shifts toward lower frequencies. Passing the symmetry point, the peaks for each direction are similar in form until they pass each other and continue their respective trends. To explain this behavior, Figs. 6(c) and 6(d) show the inversion within the gain chip QW for two of the previous simulations, where the output coupler to gain chip length was 1.751 mm [Fig. 6(c)] and 1.545 mm [Fig. 6(d)], respectively. Figure 6(c) shows that for the 1.751 mm arm length simulation, the inversion before each pulse enters is nearly identical. This indicates an equal availability of carriers for both pulses. After the pulses have passed, it is seen that the burned kinetic holes are again nearly identical. These nearly identical conditions, stabilized over thousands of round trips, led to equal pulse amplification on each pass which in turn led to the near equal pulse intensities observed for this setup. Figure 6(d) shows population inversions, 100 fs before and after the incident pulse peaks, when the gain chip was placed 1.545 mm from the OC. By moving the gain chip closer to the OC, the delay between when the CW pulse hits the QW and when the CCW pulse hits is dramatically shortened. Thus, the carriers recover much more fully for the CW pulse than for the CCW pulse. The presence of more carriers leads to deeper kinetic holes. This leads to larger pulses, which in turn burn deeper kinetic holes, further exacerbating the difference between the two distributions. Although these kinetic holes are quickly filled, the distributions cannot fully recover between passes, such that the two directions effectively see distinct background distributions. This stabilizes over thousands of round trips to form two pulses with distinct intensities. If the delay

difference is large enough, then the weaker direction does not have enough carriers to provide a net amplification to the pulse and it cannot grow beyond a certain point. This highlights that gain competition does contribute to a delicate stabilization of the pulses in either direction but it in no way leads to balanced pulses. Instead, gain dominance in one direction versus the other leads to distinct pulse intensities. Further, as the CW pulse grows in intensity it depletes greater numbers carriers at lower energies. This creates more favorable gain at higher energies for the CCW pulse, leading to a growing and nonuniform offset in their spectral peaks. This is a behavior that is only resolvable with fully microscopic models. Experimentally, this implies a strong relative pulse intensity tunability, and a moderate spectral tunability based on gain chip position, as well as the ability to make a ring cavity unidirectional by placing the gain chip and SESAM sufficiently close together. This also implies that colliding pulse mode locking in MIXSELs is not likely feasible since the gain chip is integrated with the SESAM.

Figure 7 shows the results of utilizing a longer cavity, 33.5 mm, scaled proportionally so that the gain chip is 8.76 mm from the OC and 7.73 mm from the SESAM, starting from a 2.0×10^5 V/m seed pulse in each direction. This corresponds to a repetition rate of 8.95 GHz. This is on the smaller edge of experimentally demonstrated VECSELs [37–39] and well within the range for the SESAM integrated counterpart, MIXSELs [40]. The pump intensity is increased to show the effect that overpumping has on such a cavity. Figure 7(a) shows the evolution of the
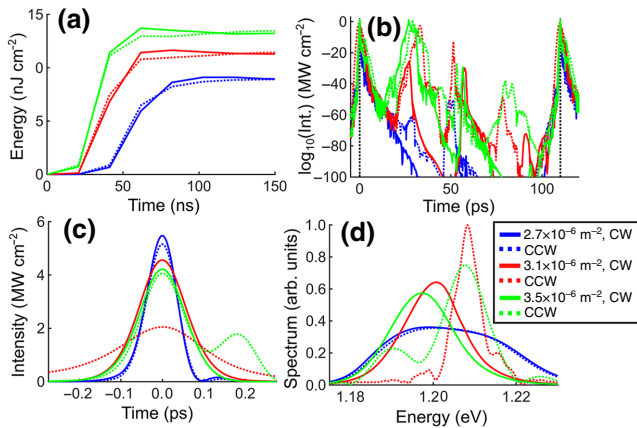

FIG. 7. Increasing pump energy through increasing carrier density comparison study for 33.5 mm ring cavity. (a) The primary pulse energy grows more rapidly at increasing densities and converges to a higher value with only modest changes in relative intensities in counterpropagating pulses. (b) The final output intensity log plot over one round trip highlighting the generation of small secondary pulses. (c) The primary pulse output intensity and (d) spectra highlighting the destabilization and shifting spectral peaks at increasing carrier densities.
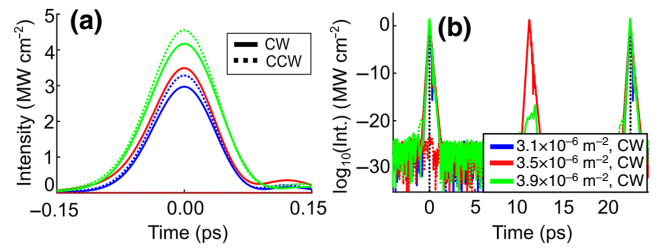

FIG. 8. A 6.7 mm ring cavity exhibits unstable unidirectionality at increasing pump powers. (a) The primary pulse output intensity profile highlights that unidirectionality exists between higher and lower pump energy bidirectional setups. (b) The log plot of output intensity over one round trip demonstrates that unidirectionality is accompanied by the generation of a secondary pulse near one-half round trip.

primary pulse output energy which grows for increasing pump powers. Note the moderate shifting in the asymptotic behavior of each of these curves. The converged fluences, ranging from 5 to 7.5 nJ/cm^{-2}, can readily be used for ultrafast pulse generation within macroscopic rate equations models [21]. Note that these values are orders of magnitude lower than saturation fluences for picosecond pulses. This is an effect of the dynamic burning, and recovery of kinetic holes which drives the populations far from Fermi distributions. Utilizing a beam waist of 336 μm, these fluences corresponds to average output powers of 79–127 mW. Previous experimental results indicate that 136 mm ring cavities can exhibit single-pulse operation up to 150–300 mW of output power, dependent on SESAM temperature [2]. The lower power limit is thought to be a byproduct of shorter pulses and higher repetition rates, as in the 100 mW single-pulse limit demonstrated for 100 fs pulses [41] or the 115 mW single-mode limit observed for a 50 GHz repetition rate. [37], both in a V-cavity setup. Figure 7(b) shows that at increasing QW carrier densities, the formation of small secondary pulses can be seen at seemingly random positions, with round trips marked by dashed black lines. Because the cavities are relatively long compared to the carrier recovery time, the carriers are almost fully recovered even at a quarter round trip. Thus, additional pulses can grow at many locations within a single round trip. However, the saturable absorber drives these secondary pulses to remain small relative to the primary pulses. This is analogous to the side-pulsing and secondary pulse formation demonstrated by Hausen *et al.* [27]. Figure 7(c) shows the converged output intensity profiles, which indicate a weakening of the peak pulse intensities with increasing pump power. This counterintuitive result is explained by the formation of these secondary pulses which saps significant carriers from the primary pulses. This leads to a decrease in available carriers for the primary pulse, leading to weaker pulses in both

directions. Further increasing the pumping power strengthens the secondary pulses and generates a strong secondary tail within the primary pulse. Interestingly, this effect leads to broader pulses with still increasing energy. Figure 7(d) shows the associated pulse spectra, indicating the splitting of the spectra so that different directions have distinct spectral peaks. At low pumping, $n_0 = 2.7 \times 10^{16}$ m^{-2}, the pulses in either direction have nearly identical broad spectra. As the pump intensity is increased, sufficient carriers are pumped into the system to provide net gain across a broader spectrum, even incorporating additional cavity modes. Thus, longer ring cavities naturally give rise to quasistable pulses with distinct spectral peaks and only weak secondary cavity pulses. The spectral shifting and resultant pulse shapes are truly microscopic results which result from the nonuniform burning and recovery of kinetic holes within the carrier populations. Experimentally, this implies that large peak wavelength shifts between the counterpropagating pulses are feasible, tunable by increasing the pump power.

Turning now to destabilizing shorter cavities, Fig. 8(a) shows the converged primary pulse intensity profiles in a 6.7 mm cavity for increasing pumping schemes. Notice that with a background density of 3.5×10^{16} m^{-2} the cavity operates unidirectionally. To identify where the excess energy is going, Fig. 8(b) shows the output intensity over one round trip on a logarithmic scale, with a round trip marked by dashed black lines. Within the unidirectional simulation, a strong harmonic pulse is generated 11 ps from, and moving in the same direction as, the primary pulse. For the higher density, only a small perturbation can be seen at this position. As the pump intensity is increased, the relative influence of the SESAM, which drives colliding pulse operation, diminishes so that multiple stable converged pulses are possible. This is an unstable equilibrium point, with increases in pump intensity reverting the setup to colliding pulse operation. This implies that unidirectional operation of a VECSEL ring cavity may be achievable through changes in pump energy alone.

B. Two-dimensional mode locking studies

The BPM within the two-dimensional cavity is setup to create a relative intensity full width at half maximum (FWHM) focus of 5 from gain chip to SESAM, as well as a total cavity length of 6.7 mm. Both gain chip and SESAM have a 2° angle of incidence upon them. The gain chip QW has a background density of 2.5×10^{16} m^{-2} with a beam waist of 336 μm and a pulse to pump spot size ratio of $w_0/w_p = 0.6$. Figure 9(a) shows the evolution of the peak pulse intensity for two gain chip positions. Unlike the one-dimensional results, for a gain chip to OC length of 1.751 mm, the pulses are nowhere near balanced, with the CW pulse being 45% stronger than the

CCW pulse. Instead, the pulses are much more closely balanced with a length of 1.442 mm which crosses the symmetry point and results in an OC to gain chip length which is 14% shorter than the gain chip to SESAM length. An interesting experimental consequence is that in order to obtain equal intensity pulses in both directions, one would likely need to adjust the chip position away from a quarter of a round trip from the SESAM, to account for bias within the setup. Figure 9(b) shows the evolution of the FWHM in time, measured about the pulse peak, for these two simulations, depicting only modest differences between the two simulations. It is worth noting that in one dimension the stronger pulse was almost uniformly the shorter pulse. In the two-dimensional studies, the pulses do not have a uniform temporal FWHM. To further examine this claim, Figs. 9(c) and 9(d) shows the converged pulse intensities for the CW beam at the output, and the total field within the QW, respectively, within the 1.442 mm OC to gain chip length simulation. The contours and color bars are shown in megawatts per square centimeter. The CW output pulse [Fig. 9(c)] is transversally symmetric and is nearly identical, up to scaling, to the CCW beam not shown. Figure 9(d) shows the total incident pulse intensity, centered on the peak of the colliding pulse intensity profile. Note the three distinct peaks, in agreement with the analytic interference fringes for in-phase pulses. This confirms that the pulses are in fact colliding and that they have naturally stabilized to maintain an in-phase relationship, as predicted in Fig. 4. The peak of the strongest interference fringe is off-centered, a result of a stronger CW pulse, relative to the CCW pulse. Figures 9(e)–9(h) show the population inversion as it evolves over the pulse interaction. Figure 9(e) shows the population inversion 30 fs before the peak of the colliding pulses. Generated carriers are visible as kinetic peaks at the spatial and spectral centers of the peaks of the pulse. At the peak of the colliding pulses [Fig. 9(f)] the kinetic peaks have shifted toward higher energies as the lower energies are saturated. As shown in Fig. 9(g), 30 fs after the pulse peak, new kinetic peaks have formed in between the previous ones. This indicates excessive absorption within the cavity as a result of nonoverlapping regions of the colliding pulses. Figure 9(h) shows the population inversion 150 fs after the peak of the colliding pulses. The multiple kinetic peaks, present only in the higher-order grating terms, have rapidly smoothed to a single central peak which slowly recovers to the background carrier distribution. The excessive absorption that occurs during this interaction not only reduces the quality of the beam but also leads to a larger interaction region on the SESAM and ultimately more rapid SESAM degradation. Thus, for minimal SESAM degradation, and uniformly short, strong pulses, ring cavity VECSELs should be designed with the minimal possible angle of incidence on the SESAM.
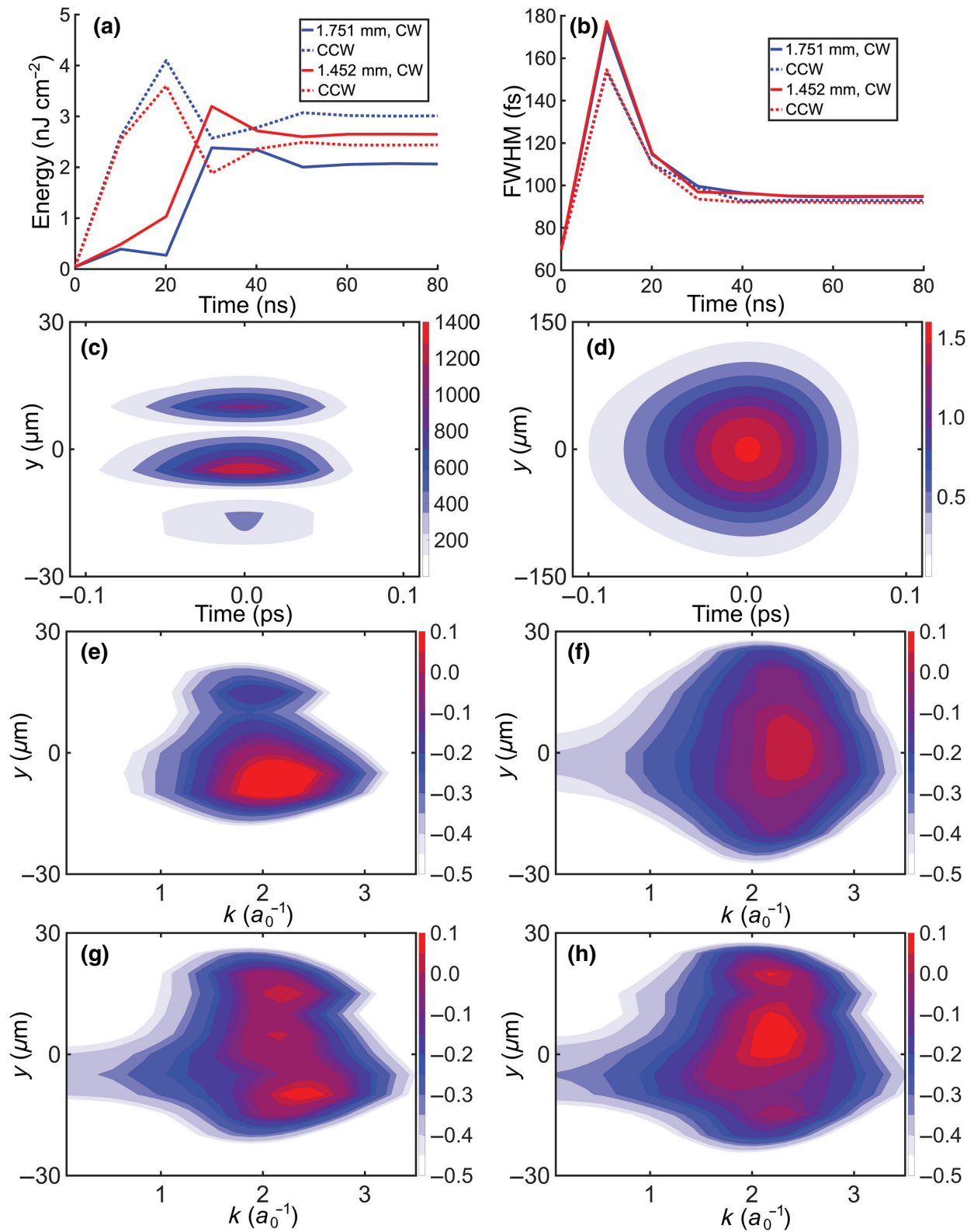
FIG. 9. (a) Output pulse energy and (b) full width at half maximum convergence for two-dimensional ring cavities with variable OC to gain chip arm lengths with a constant total length of 6.7 mm. (c) Converged output pulse intensity and (d) intensity within the SESAM QW within the 1.442 mm simulation. SESAM QW population inversions (e) 30 fs before the peak, (f) at the peak, (g) 30 fs after the peak, and (h) 150 fs after the peak.

V. CONCLUSIONS

The relative position of the gain chip has dramatic implications for the strength of the bidirectional pulses. Gain competition both allows the stabilization of pulses in either direction and prohibits their total balance. Slight biases within the cavity destabilize this equilibrium, making it likely experimentally inaccessible. Properly designing relative mode sizes between the gain chip and SESAM is vital for optimal operation either for improved pulse behaviors, or prolonged SESAM degradation with significant pulse reshaping resulting from varied foci. Longer cavities recover more readily between pulse passes, allowing the cavity to stabilize in numerous unpredictable ways when overpumped. These cavities were shown to destabilize through the amplification of distinct spectral peaks in either direction. In shorter cavities, where gain recovery time has a much stronger effect, destabilization most readily occurred at half round trip intervals. Unstable unidirectional behaviors were demonstrated. These were destroyed by changes in either chip positions or gain chip QW densities. The shifting of spectral peaks and unstable unidirectionality is directly linked to the dynamic burning and recovery of inhomogeneous kinetic holes. The macroscopic gain coupling of a particular setup is thus intimately linked to propagation direction, cavity lengths, incidence angles, and pump conditions, making predictive modeling using macroscopic methods highly restrictive. Carrier dynamics were investigated in two dimensions to demonstrate the effect of the interfering colliding pulses, highlighting the complex evolution of kinetic peaks. These kinetic peaks drive the pulses toward overlapping entirely, increasing absorption in setups with nonzero angles of incidence. Thus, minimizing angles of incidence on the SESAM is vital for producing uniformly short, strong pulses. Broadly, the careful tuning of geometrical setups and pumping within a ring cavity can provide a wealth of rich phenomena and a means of producing high- quality ultrafast pulses, driven by the underlying nonequilibrium carrier dynamics.

[1] R. L. Fork, B. I. Greene, and C. V. Shank, Generation of optical pulses shorter than 0.1psec by colliding pulse mode locking, Appl. Phys. Lett. **38**, 671 (1981).

[2] A. Laurain, D. Marah, R. Rockmore, J. McInerney, J. Hader, A. R. Perez, W. Stolz, and J. V. Moloney, Colliding pulse mode locking of vertical-external cavity surface-emitting laser, Optica **3**, 781 (2016).

[3] S. M. Link, D. Waldburger, C. G. E. Alfieri, M. Golling, and U. Keller, Coherent beam combining and noise analysis of a colliding pulse modelocked vecsel, Opt. Express **25**, 19281 (2017).

[4] M. Kuznetsov, F. Hakimi, R. Sprague, and A. Mooradian, High-power (gt;0.5-w cw) diode-pumped vertical-external-cavity surface-emitting semiconductor lasers with circular tem/sub 00/beams, IEEE Photonics Technol. Lett. **9**, 1063 (1997).

[5] P. Zorabedian, Tunable external-cavity semiconductor lasers, in *Tunable Lasers Handbook* (, 1995), p. 349.

[6] S. Calvez, J. E. Hastie, M. Guina, O. G. Okhotnikov, and M. D. Dawson, Semiconductor disk lasers for the generation of visible and ultraviolet radiation, Laser Photonics Rev. **3**, 407 (2009).

[7] K. G. Wilcox, A. C. Tropper, H. E. Beere, D. A. Ritchie, B. Kunnert, B. Heinen, and W. Stolz, 4.35 kW peak power femtosecond pulse modelocked vecsel for supercontinuum generation, Opt. Express **21**, 1599 (2012).

[8] C. Hessnius, P. Guinet, M. Lukowski, J. Moloney, and M. Fallahi, in *Proc. SPIE 8242: Vertical External-Cavity Surface-Emitting Lasers (VECSELs) II* (SPIE LASE, 2012).

[9] J. Woods, D. Heath, J. Daykin, T. C. Sverre, B. Keenlyside, B. Mills, I. Sagnes, G. Beaudoin, S. Blin, A. Garnache, A. Tropper, and V. Apostolopoulos, Semiconductor disk laser in bi-frequency operation by laser ablation micromachining of a laser mirror, Opt. Express **27**, 22316 (2019).

[10] C. A. Zaugg, A. Klenner, M. Mangold, A. S. Mayer, S. M. Link, F. Emaury, M. Golling, E. Gini, C. J. Saraceno, B. W. Tilma, and U. Keller, Gigahertz self-referenceable frequency comb from a semiconductor disk laser, Opt. Express **22**, 16445 (2014).

[11] U. Keller and A. C. Tropper, Passively modelocked surface-emitting semiconductor lasers, Phys. Rep. **429**, 67 (2006).

[12] B. W. Tilma, M. Mangold, C. A. Zaugg, S. M. Link, D. Waldburger, A. Klenner, A. S. Mayer, E. Gini, M. Golling, and U. Keller, Recent advances in ultrafast semiconductor disk lasers, Light: Sci. Appl. **4**, e310 (2015).

[13] A. Rahimi-Iman, Recent advances in VECSELs, J. Opt. **18**, 093003 (2016).

[14] M. Guina, A. Rantamäki, and A. Härkönen, Optically pumped VECSELs: review of technology and progress, J. Phys. D: Appl. Phys. **50**, 383001 (2017).

[15] A. Laurain, I. Kilen, J. Hader, A. R. Perez, P. Ludewig, W. Stolz, S. Addamane, G. Balakrishnan, S. W. Koch, and J. V. Moloney, Modeling and experimental realization of modelocked VECSEL producing high power sub-100 fs pulses, Appl. Phys. Lett. **113**, 00 (2018).

[16] T. Ochalski, A. de Burca, G. Huyet, J. Lyytikainen, M. Guina, M. Pessa, A. Jasik, J. Muszalski, and M. Bugajski, in *2008 Conference on Lasers and Electro-Optics and 2008*

Conference on Quantum Electronics and Laser Science (2008), p. 1.

[17] K. Viskontas, K. Regelskis, and N. Rusteika, Slow and fast optical degradation of the sesam for fiber laser mode-locking at 1 μm, Lithuanian J. Phys. **54,** 127 (2014).

[18] S. Addamane, D. Shima, A. Laurain, H.-T. Chan, G. Balakrishnan, and J. V. Moloney, in *Vertical External Cavity Surface Emitting Lasers (VECSELs) VIII*, Vol. 10515, edited by J. L. Chilla, International Society for Optics and Photonics (SPIE, 2018), p. 80.

[19] M. Lindberg, R. Binder, and S. W. Koch, Theory of the semiconductor photon echo, Phys. Rev. A **45,** 1865 (1992).

[20] H. A. Haus, Theory of mode locking with fast saturable absorber, J. Appl. Phys. **46,** 3049 (1975).

[21] R. Paschotta, R. Häring, A. Garnache, S. Hoogland, A. C. Tropper, and U. Keller, Soliton-like pulse-shaping mechanism in passively mode-locked surface-emitting semiconductor lasers, Appl. Phys. B: Lasers Opt. **75,** 445 (2002).

[22] A. G. Vladimirov and D. Turaev, Model for passive mode locking in semiconductor lasers, Phys. Rev. A **72,** 033808 (2005).

[23] E. A. Avrutin and K. Panajotov, Delay-differential-equation modeling of mode-locked vertical-external-cavity surface-emitting lasers in different cavity configurations, Materials **12,** 3224 (2019).

[24] A. G. Vladimirov, K. Panajotov, and M. Tlidi, Orthogonally polarized frequency combs in a mode-locked vecsel, Opt. Lett. **45,** 252 (2020).

[25] A. M. Perego, B. Garbin, F. Gustave, S. Barland, F. Prati, and G. J. de Valcárcel, Coherent master equation for laser modelocking, Nat. Commun. **11,** 311 (2020).

[26] J. Hausen, K. Lüdge, S. V. Gurevich, and J. Javaloyes, How carrier memory enters the haus master equation of mode-locking, Opt. Lett. **45,** 6210 (2020).

[27] J. Hausen, S. Meinecke, B. Lingnau, and K. Lüdge, Pulse cluster dynamics in passively mode-locked semiconductor vertical-external-cavity surface-emitting lasers, Phys. Rev. Appl. **11,** 044055 (2019).

[28] O. D. Sieber, M. Hoffman, V. J. Wittwer, M. Mangold, M. Golling, B. W. TIlma, T. Südmeyer, and U. Keller, Experimentally verified pulse formation model for high-power femtosecond vecsels, Appl. Phys. B: Lasers Opt. **113,** 133 (2013).

[29] I. Kilen, *Non-equilibrium many-body influence on mode-locked Vertical External-Cavity Surface-Emitting Lasers*, Ph.D. thesis, University of Arizona (2017).

[30] I. Kilen, J. Hader, J. V. Moloney, and S. W. Koch, Ultrafast nonequilibrium carrier dynamics in semiconductor laser mode locking, Optica **1,** 192 (2014).

[31] I. Kilen, S. W. Koch, J. Hader, and J. Moloney, Non-equilibrium ultrashort pulse generation strategies in VECSELs, Optica **4,** 412 (2017).

[32] S. McLaren, I. Kilen, and J. V. Moloney, Microscopic modeling of transverse mode instabilities in mode-locked vertical external-cavity surface-emitting lasers, Appl. Phys. Lett. **116,** 031102 (2020).

[33] S. McLaren, I. Kilen, and J. V. Moloney, Microscopic modeling of non-normal incidence vertical external cavity surface-emitting laser cavities, Appl. Phys. Lett. **118,** 121103 (2021).

[34] M. Mansuripur, *Field, Force, Energy and Momentum in Classical Electrodynamics* (Bentham Science Publishers Ltd., 2011).

[35] A. Bäumner, S. W. Koch, and J. V. Moloney, Non-equilibrium analysis of the two-color operation in semiconductor quantum-well lasers, Phys. Status Solidi B **248,** 843 (2011).

[36] J. Hader, M. Scheller, A. Laurain, I. Kilen, C. Baker, J. V. Moloney, and S. W. Koch, Ultrafast non-equilibrium carrier dynamics in semiconductor laser mode-locking, Semicond. Sci. Technol. **32,** 013002 (2016).

[37] D. Lorenser, D. J. H. C. Maas, H. J. Unold, A.-R. Bellancourt, B. Rudin, E. Gini, D. Ebling, and U. Keller, 50-GHz passively mode-locked surface-emitting semiconductor laser with 100-mW average output power, IEEE J. Quantum Electron. **42,** 838 (2006).

[38] C. G. E. Alfieri, D. Waldburger, S. M. Link, E. Gini, M. Golling, G. Eisenstein, and U. Keller, Optical efficiency and gain dynamics of modelocked semiconductor disk lasers, Opt. Express **25,** 6402 (2017).

[39] P. Klopp, U. Griebner, M. Zorn, and M. Weyers, Pulse repetition rate up to 92 GHz or pulse duration shorter than 110 fs from a mode-locked semiconductor disk laser, Appl. Phys. Lett. **98,** 071103 (2011).

[40] M. Mangold, C. A. Zaugg, S. M. Link, M. Golling, B. W. Tilma, and U. Keller, Pulse repetition rate scaling from 5 to 100 GHz with a high-power semiconductor disk laser, Opt. Express **22,** 6099 (2014).

[41] D. Waldburger, C. G. E. Alfieri, S. M. Link, S. Meinecke, L. C. Jaurigue, K. Lüdge, and U. Keller, Multipulse instabilities of a femtosecond sesam-modelocked vecsel, Opt. Express **26,** 21872 (2018).